Journal of
Materials Chemistry A

ROYAL SOCIETY
OF CHEMISTRY

PAPER

View Article Online
View Journal | View Issue

Cite this: *J. Mater. Chem. A*, 2025, **13**, 7999

Broad-spectrum photothermal high-entropy alloy powders for efficient solar-driven antibacterial and dye degradation†

Bang An,[a] Mengmeng Yang,[a] Yuanyuan Shang,[b] Chao Sun,[a] Shuo Wang,[a] Kun Qian,[a] Xuexue Zou,[a] Qiangsheng Dong,[c] Yi Shao,[ad] Chenglin Chu, [a] Feng Xue,*[a] Cheng Wang*[a] and Jing Bai *[ad]

Received 13th October 2024
Accepted 4th February 2025

DOI: 10.1039/d4ta07296k

rsc.li/materials-a

The development of solar-driven photothermal materials for efficient wastewater treatment remains a significant challenge. Herein, we have designed and synthesized a series of FeMnCo-based high-entropy alloy powders (HEAPs) with exceptional photothermal conversion, antibacterial properties and dye degradation capabilities. Under visible light irradiation, FeMnCoTiV HEAPs demonstrate a solar absorption efficiency of 85.6% across a broad solar spectrum range (200–2500 nm). This broad absorption range enables HEAPs to heat water to 45 °C, and completely degrade Orange II within 15 minutes. Furthermore, HEAPs effectively inhibit the growth of *Escherichia coli* (*E. coli*) and *Staphylococcus aureus* (*S. aureus*). Theoretical calculations of the d-band density of states (d-DOS) attribute the wide absorption range and high efficiency to the optimized distribution of 3d electrons, particularly influenced by the high proportion of Ti and V states in the alloy. The distribution which correlated with d–d interband transitions indicated that the solar absorption properties could be controlled by adjusting elemental composition. These findings not only open additional pathways for wastewater treatment but also provide insights for the composition design and industrial applications of HEAPs.

1. Introduction

Water scarcity has become one of the core issues limiting the sustainable development of human society.[1] A significant amount of untreated or inadequately treated wastewater is discharged into natural water bodies, resulting in severe environmental pollution. Achieving the recycling of wastewater not only helps to improve the environment but also significantly alleviates the pressure of water resource shortages.[2,3]

Currently, common methods for wastewater treatment include physical, biological, and chemical processes. The physical methods separate pollutants from wastewater through means such as adsorption, membrane separation, and magnetic separation. While these approaches facilitate the transfer of pollutants, they do not effectively remove them.[4–7] The biological methods rely on the metabolic activities of microorganisms to degrade dyes in wastewater, mainly including anaerobic and aerobic processes. However, these methods are significantly influenced by temperature and pH, limiting their application to dilute solutions and extending the treatment time.[8–10] The chemical methods consist of techniques that transform, break down, or remove pollutants in wastewater through chemical reactions.[11] Among these methods, advanced oxidation processes demonstrate excellent efficacy in removing persistent organic pollutants,[12,13] while electrochemical methods show promising potential in addressing heavy metal contamination. However, their applicability is often restricted due to the stringent equipment requirements of chemical methods and the potential secondary pollution from the use of related chemical reagents.[14–18] Given the limitations of existing methods, it becomes particularly important to develop new wastewater treatment materials that are easy to prepare, cost-effective, and environmentally friendly.

Among various new materials, high-entropy alloys have garnered widespread attention due to their unique structure and exceptional physicochemical properties. High-entropy alloys typically consist of at least five elements combined in equal or near-equal atomic ratios.[19,20] Common preparation methods include melting,[21] powder metallurgy,[22] and laser

---

[a] School of Materials Science and Engineering, Jiangsu Key Laboratory for Advanced Metallic Materials, Southeast University, Nanjing 211189, China. E-mail: cheng.wang@seu.edu.cn; xuefeng@seu.edu.cn; baijing@seu.edu.cn

[b] Department of Materials Design, Institute of Hydrogen Technology, Helmholtz-Zentrum Hereon GmbH, Geesthacht 21502, Germany

[c] School of Materials Science and Engineering, Nanjing Institute of Technology, Nanjing 211167, China

[d] Institute of Biomedical Devices (Suzhou), Southeast University, Suzhou, 215163, China

† Electronic supplementary information (ESI) available. See DOI: https://doi.org/10.1039/d4ta07296k

melting.[23] Among the aforementioned alloy preparation techniques, the melting method exhibits a significant advantage in achieving uniform composition when producing high-entropy alloys. In contrast, laser melting technology enables precise control over alloy shapes. On the other hand, powder metallurgy is widely used due to its relatively low cost. Their complex composition and distinctive structure confer several advantages on them over traditional alloys, including tunable compositions, diversity of reactive active sites, a significant number of unsaturated atomic coordinations, and synergistic effects among different elements.[24–28] These performance advantages allow high-entropy alloys to exhibit tremendous application potential in the field of wastewater treatment.

Despite the currently limited reports of high-entropy alloys in wastewater treatment, existing studies show promising application prospects. In 2016, Lv *et al.*[29] conducted the first study on the application of high-entropy alloys in dye degradation, manufacturing an AlCoCrTiZn high-entropy alloy through mechanical alloying. The strong reducing capability provided by the active element aluminum coupled with the characteristics of a wavy surface imparted by the milling process enables AlCoCrTiZn to demonstrate exceptional efficiency in the degradation of DB6 dye. Furthermore, doping with non-metallic elements is one of the key methods to enhance the dye degradation performance of high-entropy alloys. The incorporation of sulfur, phosphorus, and carbon greatly increases the quantity and efficiency of electron transfer for AlCrFeMnX (where X = S, P, C) compared to its parent alloy AlCrFeMn, boosting the degradation efficiency for DB6 to 42 times higher than that of the parent alloy.[30] In the core–shell material formed between CoNiCuFeMn and biochar, the abundant oxygen-containing functional groups on the surface of the biochar serve as electron donors, significantly activating peroxymonosulfate and enhancing the degradation efficiency of ofloxacin from 23.7% to 98.2%.[31]

In 2022, Wang *et al.*[32] further expanded the application of high-entropy alloys in wastewater treatment by investigating the performance of equiatomic ratio high-entropy amorphous alloys in dye degradation for the first time. The synthesized FeCoNiMnCuTi high-entropy amorphous alloy not only possesses the catalytic performance stability conferred by its amorphous structure but also fully utilizes the synergistic catalytic advantages of the various active elements found in high-entropy alloys. Under mild acidic conditions, this alloy can completely degrade Rhodamine B within only 8 minutes, achieving a degradation efficiency that exceeds that of all previously reported alloy catalysts. Additionally, related studies have found that the reduction of adsorbed oxygen molecules at active sites by photogenerated electrons can effectively stimulate the photocatalytic performance of MnFeCoNiCu, thereby facilitating the efficient degradation of antibiotics such as organic carbon, sulfameth, oxazole and ofloxacin.[33] These studies collectively indicate that high-entropy alloys have excellent performance and broad application prospects for removing organic and inorganic pollutants in wastewater.

It is important to note that current research on wastewater treatment materials mainly focuses on the removal of organic and inorganic pollutants, often overlooking the impact of microorganisms. The presence of microorganisms can not only damage the performance of materials but also pose a threat to human health.[34] Unfortunately, materials capable of simultaneously achieving dye degradation and antibacterial functionality remain relatively scarce. Recent studies have indicated that high-entropy alloys exhibit excellent antibacterial properties,[35,36] positioning them as a promising candidate for wastewater treatment materials that combine both sterilization and degradation functions. However, existing antibacterial high-entropy alloys typically require the incorporation of antibacterial elements such as copper or silver, which limits the flexibility of compositional design. Photothermal materials have the ability to effectively convert light energy into thermal energy through their outstanding photothermal conversion performance, thereby imparting antibacterial properties to otherwise non-antibacterial materials. For example, gold nanoparticles can release heat under 808 nm laser irradiation, effectively killing cancer cells and inhibiting corresponding solid tumors and liver metastases.[37] Furthermore, semiconductor copolymer nanoparticles with broader spectral absorption capabilities can absorb not only 808 nm wavelength laser light but also effectively absorb 1064 nm wavelength laser light, enhancing the ablation effect on cancer cells.[38]

Despite the favorable photothermal antibacterial performance of these materials, they generally suffer from a narrow light absorption range, typically only capable of absorbing near-infrared or ultraviolet light, and exhibit relatively low photothermal conversion efficiencies, failing to efficiently utilize the energy from the entire solar spectrum. Thanks to the unique lattice distortion characteristics of high-entropy alloys, these materials exhibit exceptional photothermal conversion performance. Additionally, their complex and diverse elemental combinations enhance their ability to absorb across the entire solar spectrum. This solar-driven high-entropy alloy photothermal material not only imparts good antibacterial properties to copper-free high-entropy alloys but also enhances the efficiency of dye degradation.[30]

Given the significant advantages of high-entropy alloy photothermal materials, the development of high-entropy alloys that possess combined antibacterial, dye degradation, and excellent solar spectrum absorption properties is particularly crucial for comprehensive wastewater treatment and for expanding the compositional design concepts of high-entropy alloys.

In this study, a series of FeMnCo-based high-entropy alloy powders (HEAPs) were synthesized *via* mechanical alloying. The mechanical alloying method has potential for large-scale production due to its low equipment requirements, simple operation, and cost-effectiveness. The synthesized HEAPs can serve as a solar-driven photothermal material for eliminating bacteria and removing organic pollutants in wastewater. This study also combines density functional theory (DFT) with traditional characterization techniques (SEM, TEM, *etc.*) to cross-validate findings and deeply explore the electronic structure of the alloys, effectively clarifying the mechanisms that influence material performance. The HEAPs with photothermal characteristics provide another approach for achieving highly efficient wastewater treatment, with the potential to promote the widespread application of HEAPs in addressing environmental pollution issues for sustainable development.

2. Experimental

2.1. Preparation of HEAPs

The raw materials used in the experiment consisted of HEAPs of Fe, Co, Mn, Ni, Ti, V, Cr, and Cu, with a purity greater than 99.8% and an approximate particle size of 50 μm. The HEAPs with different compositions were prepared through mechanical alloying using a comprehensive planetary ball mill (QM-QX2) set at a rotation speed of 300 rpm. The mass ratio of the balls to the powder was maintained at 10 : 1, with a ball size ratio of 1 : 2 between the larger balls (10 mm) and the smaller balls (6 mm). The multi-stage mechanical alloying process involved a combination of dry and wet milling. Initially, the powder underwent dry milling for 60 hours, followed by the addition of 30 milliliters of anhydrous ethanol as a process control agent for wet milling, which lasted for 4 hours. To prevent overheating, a 30 minutes pause was implemented after every 30 minutes of milling, during which the rotation direction was changed. To avoid oxidation of the powder during milling, the milling jars were vacuumed and then filled with high-purity argon gas as a protective atmosphere before both the dry and wet milling processes. After wet milling, the obtained powder was dried in a vacuum oven at 100 °C for 24 hours to remove any residual ethanol. The detailed preparation process is shown in Fig. 1.

2.2. Photothermal test

100 mg of the HEAPs was placed in a beaker containing 50 mL of water. Under controlled room temperature conditions of 23 °C, a 300 W xenon lamp was placed directly above a beaker and the sample irradiated for 60 min. The temperature changes of the water in the beaker were recorded in real time using a Fluke TiX580 infrared thermal imaging camera, with a distance of approximately 20 cm between the light source and the sample. Additionally, another 100 mg sample of the powder was placed on an insulating plastic plate, while keeping the other experimental conditions the same, to test the temperature changes of the HEAPs in the air. The temperature readings were corroborated with a TA603A thermometer to ensure accuracy. Each heating and cooling cycle was repeated at least 3 times to validate the data reliability.

2.3. Antibacterial test

The antibacterial performance of HEAPs was evaluated using *E. coli* and *S. aureus*. The bacteria were inoculated in nutrient broth and cultured at a constant temperature of 37 °C for 24 hours. The bacterial liquid was then diluted with phosphate-buffered saline (PBS) to obtain a bacterial suspension with the desired concentration. Sterilized 20 mg of HEAPs was added to 10 mL of the bacterial suspension in a 6-well cell culture plate for co-culturing. The plate was placed in a 37 °C incubator for 24 hours. During this period, the samples were taken out and exposed to a 300 W xenon lamp for 60 min, labeled as the light group, while the samples that were not taken out for light exposure were labeled as the dark group. After the incubation, 100 μL of the bacterial liquid was spread onto agar plates and incubated at 37 °C, where the growth of colonies from different samples was observed and recorded. The formula for calculating the antibacterial rate is as follows:

$$\text{Antibacterial rate }(\%) = (A_{\text{ctrl}} - A_{\text{anti}})/A_{\text{ctrl}} \times 100\% \tag{1}$$

where A_{ctrl} is the number of bacteria attached to the surface of HEAPs (control group), and A_{anti} is the number of bacteria attached to the surface of HEAPs in the light group.

2.4. Dye degradation

In the dye degradation experiment, the amount of HEAPs was 2 g L^{-1}, and the concentration of the Orange II dye solution was 20 mg L^{-1}. A total of 0.5 g of HEAPs was added to 250 mL of the Orange II solution for keeping the ratio between the amount of HEAPs and the concentration of the Orange II the same in parallel experiments. Before adding HEAPs to the Orange II dye solution, the HEAPs were screened through a 200-mesh sieve to remove larger particles, effectively reducing the tendency of the powder to settle at the bottom of the beaker. The beaker was placed in a constant temperature water bath at 30 °C, with a mechanical stirring speed of 350 rpm for the constantly uniform mixture between HEAPs and Orange II dye solution. The stirring blades were also kept close to the bottom of the beaker for preventing powder from settling at the bottom of the beaker. At regular intervals, approximately 3 mL of the solution was quickly taken from the beaker using a syringe, filtered through a 0.45 μm membrane, and then tested using a Cary 5000 UV-Vis-NIR spectrophotometer. This experiment was divided into dark and light groups. The dark group was examined in a dark environment throughout the entire degradation

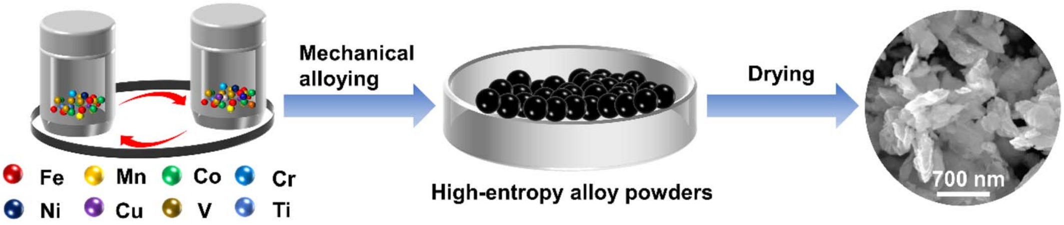

Fig. 1 Schematic illustration for the preparation of high-entropy alloy powders (HEAPs).

process. The light group was irradiated with a 300 W xenon lamp for 60 min, while the other experimental conditions remained the same as those in the dark group. At least three parallel samples were tested to ensure the accuracy and reproducibility of the experimental results.

2.5. Characterization

The phase analysis of the powders was performed using a D8-discover X-ray diffractometer, with a scanning range of 10–80°. The morphology and elemental mapping of the powders were observed using a Crossbeam 350 scanning electron microscope (SEM) with energy dispersion spectra (EDS) capability. The solar absorption properties of the materials were characterized using a Cary 5000 UV-Vis-NIR spectrophotometer. Additionally, the temperature changes of materials under 300 W xenon lamp irradiation were recorded in real time using a FLUKE Ti500 infrared thermal imaging camera. Reactive oxygen species (ROS) were detected using Electron Paramagnetic Resonance (EPR) spectroscopy (EMXplus 9.5/12), with the spin trap 5,5-dimethyl-1-pyrroline-*N*-oxide (DMPO) as the capturing agent. The cumulative release of Cu^{2+} was tested using Inductively Coupled Plasma Optical Emission Spectroscopy (ICP-OES, Thermo Scientific ICP 650). The particle size distribution of the HEAPs was measured using a laser scattering particle size distribution analyzer (S3500). The chemical reaction groups were identified using Fourier transform infrared spectrometry (FTIR, Nicolet iS10, Thermo Scientific, USA). The chemical states of the material's surface were characterized using XPS technology (XPS-2, POLAND).

2.6. Theoretical simulations

The structure of the HEAPs was calculated using the Vienna *Ab initio* Simulation Package (VASP) software based on DFT. The electronic structures are described using the generalized gradient approximation (GGA)-based Perdew–Burke–Ernzerhof (PBE) exchange–correlation functional in conjunction with the projector augmented wave (PAW) method. The cutoff energy was set to 400 eV, and the unit cell containing 108 atoms is built for the calculation. With energy convergence requirements of 1×10^{-4} eV per atom, the structures were relaxed until the forces acting on all atoms were less than 0.02 eV Å^{-1}. The Brillouin zone integration was performed with $2 \times 2 \times 2$ Monkhorst–Pack *k*-point sampling for the structure.

3. Results and discussion

3.1. Microstructure characterization

Nineteen different compositions of high-entropy alloy powders were synthesized using mechanical alloying. The EDS of Fig. 2(a–e) and (S1–S3)† indicate that the elemental distribution in all samples is uniform, with no significant elemental segregation or phase separation observed. In Fig. 2(k), the elements in all samples underwent sufficient diffusion, resulting in the formation of a solid solution structure. These results suggest that all samples prepared in this study are HEAPs after 60 hours of mechanical alloying. The particle size distribution indicates that compared to the approximately 50 μm particle size of the raw materials, the particle sizes of the mechanically alloyed powders are reduced, with the FeMnCoTiV high-entropy alloy powder having the smallest particle size of approximately 1.8 μm (Fig. 2(f–j)).[39,40]

3.2. Solar absorption properties

The solar spectral absorption properties of the HEAPs were studied using a UV-Vis-NIR spectrophotometer in the wavelength range of 200–2500 nm. Fig. 3(a–g) show that HEAPs with excellent solar absorption properties can be obtained by adjusting the elemental composition. The solar absorption rates of most HEAPs exceed 80% across the entire solar spectrum, with the FeMnCoTiV HEAPs exhibiting the highest average absorbance, surpassing 85.6%. With the increase in the number of principal elements, from the quaternary alloy to the quinary alloy, the solar absorption performance of the HEAPs enhanced. However, when the number of principal elements continued to increase to six, seven, and eight, the solar absorption performance gradually declined.

Fig. 3(f) shows the components with the best solar absorption performance among different principal element alloys. It is indicated that Ti can enhance solar absorption under UV light, while V can enhance solar absorption under visible light.[41,42] The least effective solar absorption performance is observed for FeMnCoCrNi in the quinary HEAPs (Fig. 3(b)) and FeMnCoCrNiCu in the senary HEAPs (Fig. 3(c)); both of these lack Ti and V elements. In contrast, the alloys with the best solar absorption performance among the quinary, senary, and septenary HEAPs are FeMnCoTiV, FeMnCoTiVCu, and FeMnCoTiVCrNi, all of which contain both Ti and V elements. Selecting elements with excellent solar absorption properties for alloying can help improve the solar absorption performance of high-entropy alloys, and this compositional selection strategy aligns with the "cocktail effect" of high-entropy alloys.[19]

To evaluate the solar absorption performance of HEAPs under solar irradiation, FeMnCoTiV HEAPs were added to a beaker filled with water; the dosage of the high entropy alloy powder was 100 mg per 50 mL of deionized water, which ensured uniform dispersion of the powder in the beaker and thus ensured the accuracy of the experiment. At the same time, we used a 300 W xenon lamp to simulate sunlight and employed an infrared thermal imager to record the temperature changes. As shown in Fig. 3(h), after 60 min of illumination, the temperature of the water increased from 23 °C to 33 °C. When the HEAPs were added, the temperature of the water rose to 45 °C, resulting in an increase of 12 °C compared to the former case. This demonstrates that the HEAPs still exhibit significant photothermal effects in water. When we transferred the experimental environment from the beaker to the air while keeping other conditions unchanged, the surface temperature of the sample could increase to about 50 °C within 120 seconds. After removing the light source, the temperature of the sample could rapidly decrease from 58 °C to room temperature within 210 seconds, indicating that the material has a quick response to light (Fig. 3(i)).

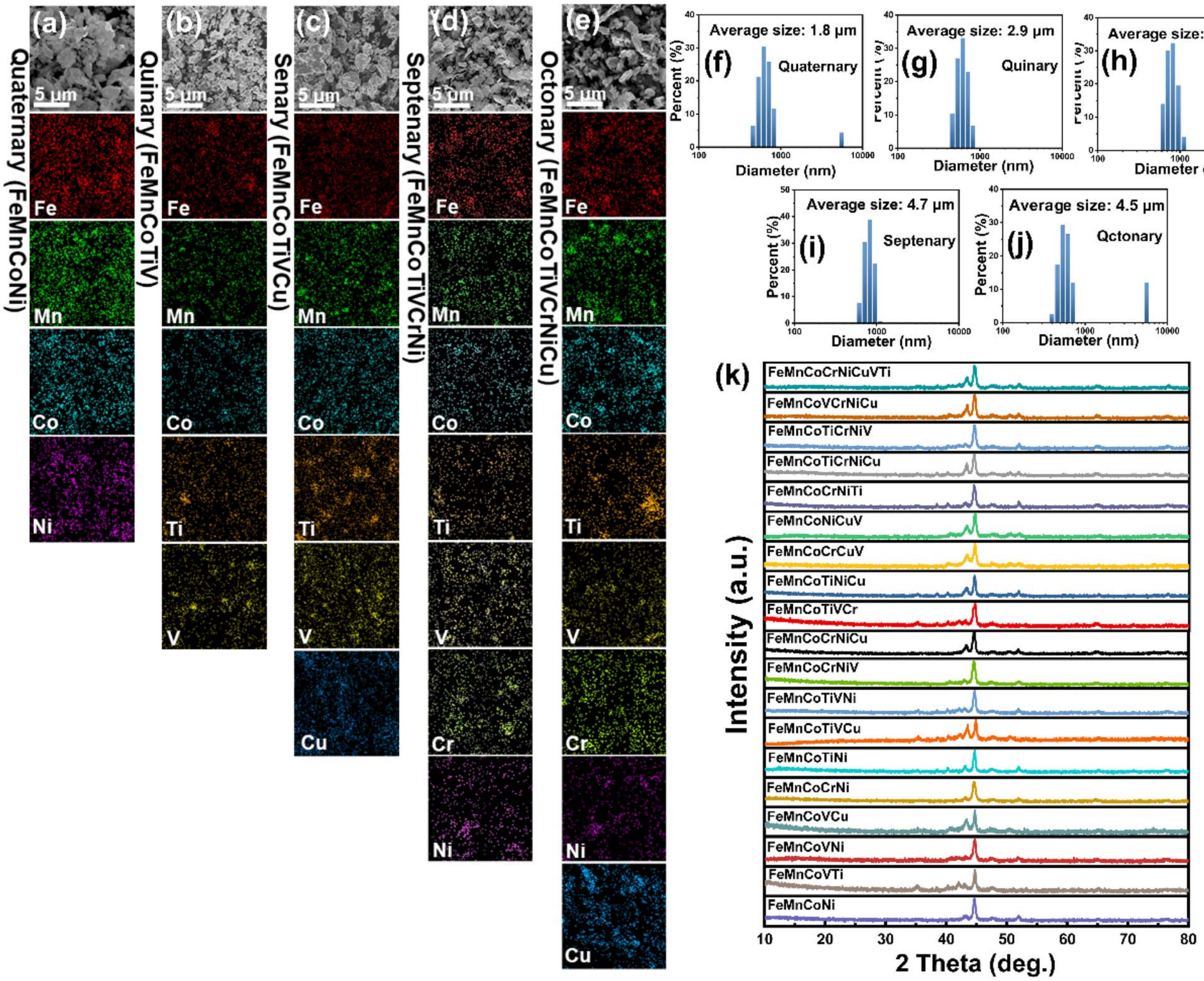

Fig. 2 Characterization of the microstructure of different HEAPs. (a)–(e) SEM images and the corresponding EDS spectra, (f)–(g) particle size distributions, and (k) XRD patterns of quaternary (FeMnCoNi), quinary (FeMnCoTiV), senary (FeMnCoTiVCu), septenary (FeMnCoTiVCrNi), and octonary (FeMnCoTiVCrNiCu) HEAPs.

The FeMnCoTiV HEAPs with the best solar absorption performance from this work are also compared with recently reported solar-absorbing materials (Fig. 4).[43–46] The FeMnCoTiV HEAPs demonstrate exceptional solar absorption capability across the entire solar spectrum (200–2500 nm), with both their absorption range and absorption rate surpassing those of most solar-absorbing materials, including graphite, only following high-entropy oxides $(Co,Mn,Fe,Cr,Ni)_3O_4$. However, compared to high-entropy oxides, high-entropy alloys exhibit higher photothermal conversion efficiency, undoubtedly providing a broader outlook for their future development.

3.3. Antibacterial properties

E. coli and *S. aureus* were co-cultured with HEAPs for 24 hours, followed by irradiation with a 300 W xenon lamp to simulate sunlight for 60 min. The antibacterial performance was then studied using the plate counting method.[47]

As shown in Fig. 5 under dark conditions, FeMnCoNi, FeMnCoTiV, and FeMnCoTiVCrNi HEAPs did not demonstrate significant antibacterial effects against *E. coli* and *S. aureus*. In contrast, the FeMnCoTiVCu and FeMnCoTiVCrNiCu HEAPs exhibited excellent antibacterial effects, with antibacterial rates exceeding 99% for both types of bacteria. When light exposure increased, the growth of the dark group bacteria was not significantly affected, while the antibacterial performance of all tested HEAPs was significantly enhanced. Fig. 5(b) illustrates the antibacterial effects of all samples against *E. coli* and *S. aureus*. Under the irradiation conditions of a 300 W xenon lamp, the antibacterial rates of FeMnCoNi, FeMnCoTiV, and FeMnCoTiVCrNi HEAPs against *E. coli* were all no less than 80.5%, while their antibacterial rates against *S. aureus* were also no less than 74.5%. Furthermore, FeMnCoTiVCu and FeMnCoTiVCrNiCu HEAPs demonstrated antimicrobial rates reaching 100% against both *E. coli* and *S. aureus*.

When the HEAPs came into contact with the bacterial solution, FeMnCoTiVCu and FeMnCoTiVCrNiCu HEAPs released Cu ions. The positively charged Cu ions can combine with the negatively charged bacteria through electrostatic forces, disrupting the bacterial cell wall. Additionally, Cu ions can

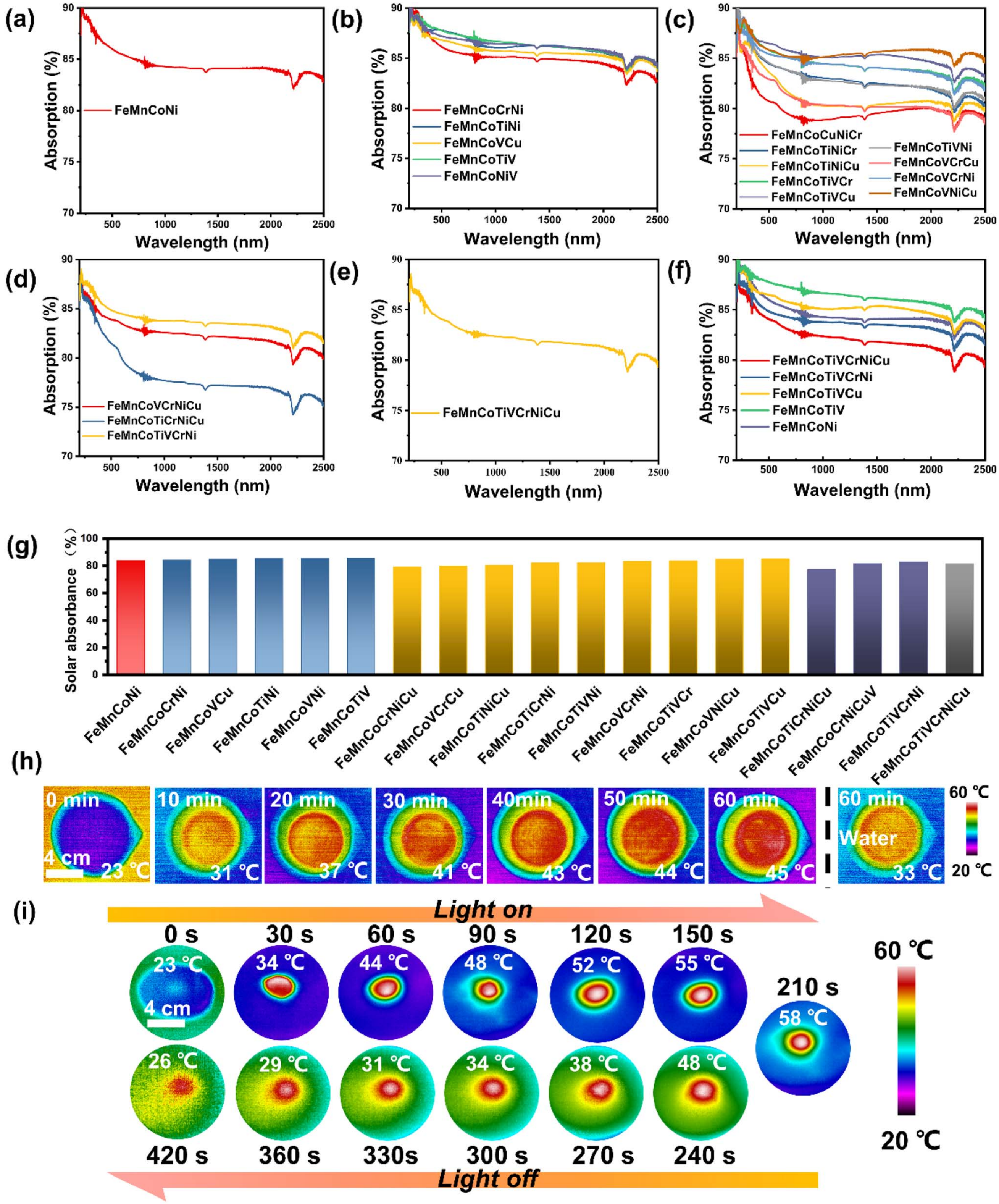

Fig. 3 Solar absorption performance of all the samples in UV-Vis-NIR regions. (a) Quaternary HEAPs. (b) Quinary HEAPs. (c) Senary HEAPs. (d) Septenary HEAPs. (e) Octonary HEAPs. (f) The best solar absorption performance among different principal element HEAPs. (g) Average solar absorbance of all samples across the entire solar spectrum. (h) FeCoMnTiV placed in a water-filled beaker and infrared images of the water temperature changes captured under 300 W xenon lamp illumination. (i) FeCoMnTiV placed on an insulating plastic board and infrared images of the surface temperature changes of the powder captured under 300 W xenon lamp illumination.

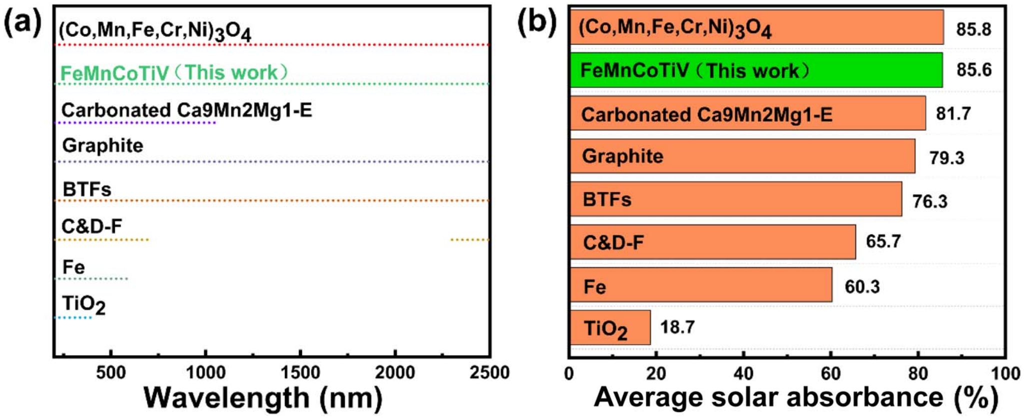

Fig. 4 Comparison of the solar absorption properties of the reported materials. (a) The area where the absorbance is no less than 70% across the entire solar spectrum. (b) The average solar absorption rate under the entire solar spectrum.

effectively catalyze oxidases and generate ROS,[48] leading to the denaturation of bacterial proteins and inhibiting bacterial growth and reproduction. Thus, FeMnCoTiVCu and FeMnCoTiVCrNiCu HEAPs exhibit excellent antibacterial effects against *E. coli* and *S. aureus* even without light assistance. The ICP test results indicate that after co-culturing with bacteria for 24 hours in a dark environment, the concentration of Cu ions released by FeMnCoTiVCu HEAPs was 7.4 mg L^{-1}, higher than the 4 mg L^{-1} released by FeMnCoTiVCrNiCu HEAPs (Fig. 5(c)). When the environment shifted to light, the concentration of Cu ions

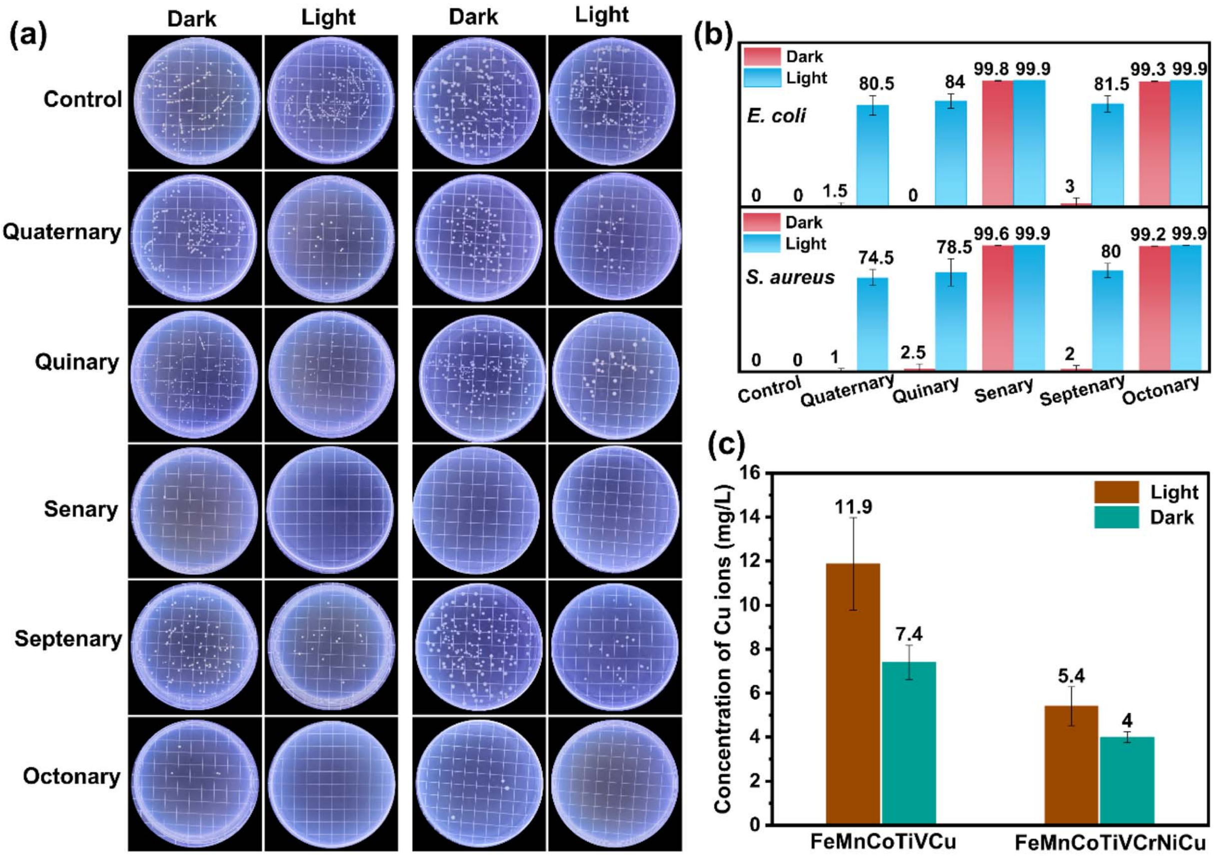

Fig. 5 Antibacterial properties of HEAPs. (a) Images of bacterial colonies of *E. coli* and *S. aureus* co-cultured with quaternary (FeMnCoNi), quinary (FeMCoTiV), senary (FeMnCoTiVCu), septenary (FeMnCoTiVCrNiCu), and octonary (FeMnCoTiVCrNiCu) HEAPs. Exposure under dark conditions indicates a light-free environment, while exposure under light conditions refers to 60 minutes of exposure to a 300 W xenon lamp. (b) Statistical results of the antibacterial rates of HEAPs. (c) Concentration of copper ions released from FeMnCoTiVCu and FeMnCoTiVCrNiCu after 24 hours of incubation in a bacterial suspension.

released by FeMnCoTiVCu HEAPs was even more significantly higher than that of FeMnCoTiVCrNiCu HEAPs. In general, FeMnCoTiVCu HEAPs demonstrated the best antibacterial performance among all tested samples.[36]

When the temperature reaches 42 °C, bacteria suffer irreversible tissue damage, and if the temperature exceeds 45 °C, rapid inactivation and death of the bacteria occur.[49] According to the experimental results shown in Fig. 3(h), after introducing light exposure, the temperature of the dark group bacterial solution only rose to 33 °C, at which temperature the bacteria can reproduce normally. HEAPs are excellent photothermal materials capable of efficiently converting light energy into heat energy. After adding HEAPs to the bacterial solution and exposing them to light for 60 min, the temperature of the solution rose to 45 °C, resulting in a significant amount of bacterial death in this temperature environment. It is noteworthy that the antibacterial effect of the HEAPs against *E. coli* is stronger than that against *S. aureus*, as *S. aureus* has a greater tolerance to high temperatures compared to *E. coli*.

3.4. Degradation experiment of orange II

Organic pollution is one of the main causes of water pollution.[50] To ensure the balance between the Orange II dye and the alloy, we adopted the parameters commonly used in most degradation experiments.[51–53] Orange II, as a typical azo dye, poses a serious threat to the ecological environment due to its presence in water bodies. To assess the potential of prepared HEAPs for environmental remediation, this study employed Orange II for degradation performance testing. Fig. 6 displays a comparison of the removal effects of different HEAPs on Orange II dye, where all the HEAPs demonstrated degradation effects on Orange II dye.

It is noteworthy that under photolytic conditions, the degradation effects of the various alloys were enhanced to varying degrees. In the absence of light, the degradation rates of Orange II after 60 min were 40%, 46%, and 66% for FeMnCoNi, FeMnCoTiV, and FeMnCoTiVCrNi HEAPs, respectively. The Cu-containing FeMnCoTiVCu and FeMnCoTiVCrNiCu HEAPs can achieve complete degradation of Orange II dye. Among them, the FeMnCoTiVCu high-entropy alloy exhibits the best performance, achieving a degradation rate of over 97% in just 15 minutes. This degradation efficiency is five times that of the $Fe_{78}Si_{13}B_9$ amorphous alloy,[54] and four times that of the Cu-T catalysts.[51]

Fig. 6(f–k) show a comparison of the degradation effect of FeMnCoTiVCu and FeMnCoTiVCrNiCu HEAPs on Orange II. The concentration of Orange II is directly proportional to the absorbance peak intensity at a wavelength of 484 nm; therefore, changes in the intensity of the absorbance peak at 484 nm can be used to indicate the degree of dye degradation. For both FeMnCoTiVCu and FeMnCoTiVCrNiCu HEAPs, in a dark environment, the absorbance peak at $\lambda = 484$ nm gradually decreases with increasing degradation time (Fig. 6(f and i)). Under 300 W xenon lamp irradiation, the rate of decrease in the absorbance peak is slightly enhanced (Fig. 6(g and j)). FeMnCoTiVCu HEAPs achieve a decolorization rate of 94% for Orange II within approximately 7 minutes while FeMnCoTiVCrNiCu HEAPs require more than 30 minutes (Fig. 6(h and k)). At the 30 minutes mark, both the illuminated and dark groups of FeMnCoTiVCu HEAPs exhibit a degradation rate of 99% for Orange II, whereas both the illuminated and dark groups of FeMnCoTiVCrNiCu HEAPs show a degradation rate of 93%. This difference is primarily because the increase in temperature only affects the degradation rate of the HEAPs towards Orange II, without impacting the degree of degradation.[55]

In the entire process of degrading Orange II dye with HEAPs, it is particularly noteworthy that the ultraviolet-visible spectra did not show any new absorption peaks (Fig. 6(f–j)), indicating that the Orange II dye has been completely degraded or adsorbed by the HEAPs.[56]

To further investigate the degradation mechanism, we employed EPR technology to capture $^{\bullet}OH$ and $^{\bullet}O_2^-$ (Fig. 7(a and b)). Under dark conditions, FeMnCoTiVCu and FeMnCoTiVCrNiCu released only trace amounts of hydroxyl radicals and superoxide radicals, whereas under illumination, a large number of hydroxyl and superoxide radicals were generated. Considering that the degradation efficiencies of Orange II by FeMnCoTiVCu and FeMnCoTiVCrNiCu remained almost unchanged under both dark and light conditions, it suggests that the roles of hydroxyl radicals and superoxide radicals in the degradation process of Orange II dye by HEAPs are minimal. Therefore, the HEAPs utilized in this study likely primarily rely on an adsorption mechanism for the degradation of Orange II. Fourier-transform infrared spectroscopy (FTIR) analyses of the Orange II solutions before and after degradation showed no new absorption peaks detected under either dark or illuminated conditions (Fig. 7(c)), indicating that no new substances were formed, which further supports the claim that the primary degradation mechanism is adsorption.

Copper, being an element with high Fenton activity, exhibits a limited degradation effect on Orange II when used alone.[57] However, due to its relatively high standard electrode potential (+0.34 V), copper can form micro-galvanic cells with elements of lower standard electrode potential within the alloy. These micro-galvanic cells significantly increase the rate of electron transfer, releasing cations with substantial positive charges.[58] These cations then combine with negatively charged Orange II dye molecules through electrostatic adsorption, leading to effective degradation of Orange II. Thus, FeMnCoTiCu and FeMnCoTiVCrNiCu show excellent degradation performance against Orange II.

According to the Nernst equation, in alloy systems containing iron, nickel, and cobalt, the standard oxidation potential of Fe/Fe^{2+} (−0.44 V) is more negative than that of H/H^+ (−0.34 V). This characteristic limits the electron transfer between cobalt or nickel and hydrogen, resulting in a reduced number of positive charges participating in electrostatic adsorption.[53,54] Consequently, the degradation efficiency of Orange II dye by FeMnCoNi HEAPs is poor compared to all other samples. In the FeMnCoTiVCrNi HEAPs, reducing nickel content improves degradation performance. Additionally, the presence of chromium promotes the formation of an oxide layer on the alloy surface, reducing the contact between active elements and dye

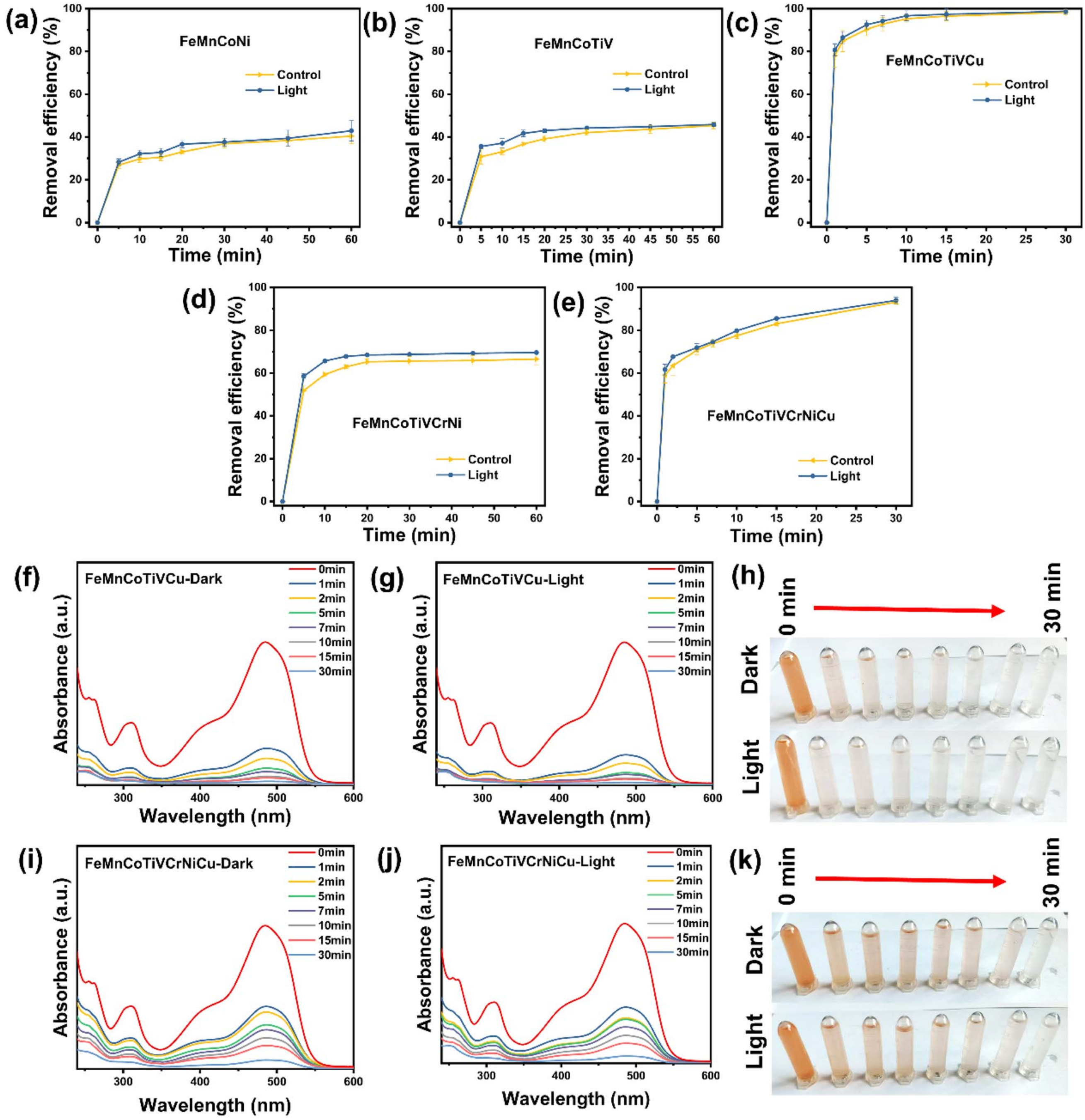

Fig. 6 Azo dye degradation efficiency of the HEAPs: the dark indicates exposure in a dark environment, while light refers to exposure to a 300 W xenon lamp. The samples are as follows: (a) FeMnCoNi, (b) FeMnCoTiV, (c) FeMnCoTiVCu, (d) FeMnCoTiVCrNi, and (e) FeMnCoTiVCrNiCu. (f) UV-Vis absorption spectra corresponding to the degradation of Orange II by FeMCoTiVCu in a dark environment. (g) UV-Vis absorption spectra of the degradation of Orange II by FeMCoTiVCu under 300 W xenon lamp irradiation. (h) Color changes of Orange II before and after degradation by FeMCoTiVCu. (i) UV-Vis absorption spectra corresponding to the degradation of Orange II by FeMCoTiVCrNiCu in a dark environment. (j) UV-Vis absorption spectra of the degradation of Orange II by FeMCoTiVCrNiCu under 300 W xenon lamp irradiation. (k) Color changes of Orange II before and after degradation by FeMCoTiVCrNiCu.

molecules, which leads to the degradation performance of FeMnCoTiVCrNiCu being inferior to that of FeMnCoTiVCu HEAPs (Fig. 6(c and e)).

Furthermore, compared to traditional cast alloys, HEAPs prepared by mechanical alloying exhibit a unique wavy surface that significantly increases the specific surface area of the alloy.[59] During degradation, the surface of the HEAPs can erode to form a porous sponge-like structure,[30,60] which not only has excellent adsorption capacity for Orange II dye but also shortens the electron transfer distance during degradation,[22] thereby

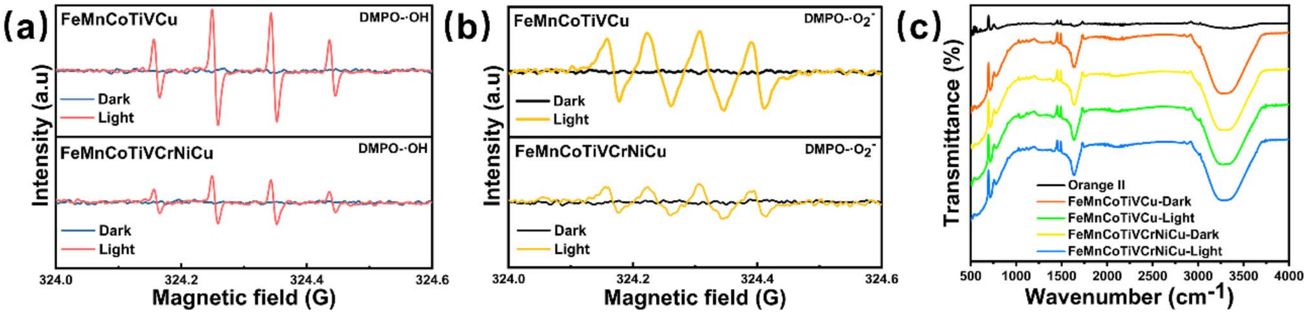

Fig. 7 After 5 minutes of visible light irradiation or in a dark environment, EPR signals of DMPO-O_2^- adducts and DMPO-OH adducts were generated by HEAPs (a) FeMnCoTiVCrNiCu and (b) FeMnCoTiVCu. (c) The FTIR of Orange II solution after reacting with HEAPs for 30 minutes.

further enhancing the degradation efficiency towards dye molecules.[61]

Temperature has a positive effect on the reaction rate of dye degradation.[62] The use of a 300 W xenon lamp as a light source to illuminate the Orange II solution containing HEAPs significantly increased the degradation efficiency of all HEAPs against Orange II. As excellent photothermal materials, HEAPs are capable of effectively converting the light energy from the xenon lamp into thermal energy, thus raising the overall temperature of the solution. The temperature increase enhances the thermal motion of dye molecules in the solution, significantly improving the effective collision frequency between dye molecules and HEAPs or other reactive species, thereby accelerating the rate of dye degradation reactions and enhancing the degradation effect of HEAPs on the dye.[63,64] Additionally, due to partial oxidation of the powder surface during ball milling, which imparts semiconductor properties, illumination can generate $^\bullet$OH and $^\bullet O_2^-$, reducing Orange II dye molecules to H_2O and CO_2.[65]

To further evaluate the application prospects of FeMnCoTiVCu HEAPs, we tested their degradation performance on Orange II dye molecules under different dye concentrations, pH values, and powder dosages, and conducted three cycling degradation tests. After the third degradation cycle, we conducted antibacterial tests using the obtained powders (Fig. 8). The results indicate that FeMnCoTiVCu still demonstrates excellent degradation performance under various conditions.

Whether the concentration of Orange II dye is increased to 80 mg L^{-1}, the powder dosage is reduced to 1 g L^{-1}, or the pH value is altered, FeMnCoTiVCu can still rapidly degrade Orange II dye molecules. The degradation rate of Orange II dye molecules by FeMnCoTiVCu gradually decreases with increasing pH. Specifically, at a pH of 3, the degradation rate constant (k) for FeMnCoTiVCu is 0.739, whereas it declines to 0.422 when the pH rises to 11.

Through pH titration, we determined that the pH_{zpc} of FeMnCoTiVCu is 8.8. This indicates that the FeMnCoTiVCu photocatalyst carries a positive charge when the pH is below 8.8 and a negative charge when the pH exceeds this value. Consequently, when the pH is below 8.8, the positively charged FeMnCoTiVCu can effectively adsorb negatively charged anions (SO_3^-) from the Orange II dye molecules. As the pH decreases, the amount of positive charge on the FeMnCoTiVCu surface

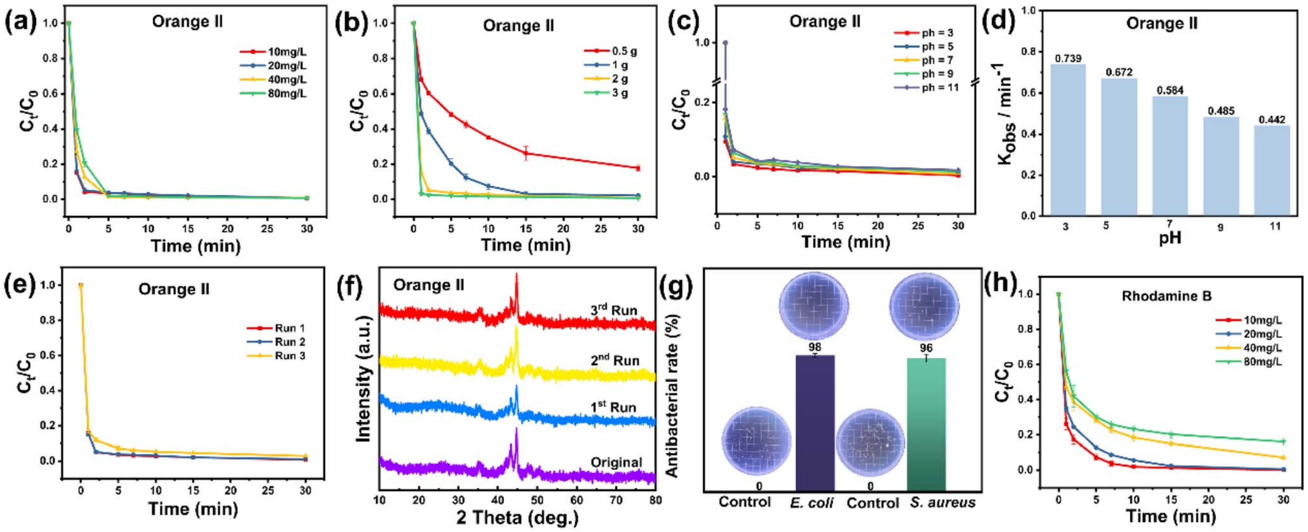

Fig. 8 The degradation efficiency of FeMnCoTiVCu HEAPs for orange deep dye under different conditions: (a) varying dye concentrations; (b) different amounts of powder; (c) different pH values; (d) K value under different pH environments; (e) cyclic performance; (f) XRD with different degradation cycle counts; (g) antimicrobial properties of the HEAPs after the third cycle; (h) the degradation efficiency of Rhodamine B.

increases, which enhances its adsorption capacity for anions (Fig. 8(a–d)).

We performed XRD tests on the powders after different degradation cycles, and the results showed no significant changes in the XRD peaks, which is consistent with our previous conclusion that the degradation mechanism of the FeMnCoTiVCu HEAPs for Orange II dye is based on adsorption (Fig. 8(e and f)). Additionally, we also tested the degradation performance of FeMnCoTiVCu on Rhodamine B dye and found that its degradation efficiency at a concentration of 80 mg L^{-1} was 92%, slightly lower than that of Orange II dye.

We believe this difference can be attributed to the inherent charge characteristics of the dyes: Orange II is an anionic dye, while Rhodamine B is a cationic dye. This results in stronger adsorption of Orange II by the positively charged FeMnCoTiVCu, thereby enhancing its degradation efficiency[33] (Fig. 8(h)). Next, we conducted antibacterial tests on the FeMnCoTiVCu HEAPs after three cycles, and the results showed antibacterial rates of 98% and 96% against *E. coli* and *S. aureus*, respectively (Fig. 8(g)).

After the degradation reaction, the main elements remaining on the surface were Fe, Mn, Co, Ti, V, Cu, and O (Fig. 9). The content of Fe significantly decreased, and the Fe^0 peak disappeared,[66] indicating that Fe may have acted as an electron donor during the dye degradation process (Fig. 9(a)). In contrast, the changes in Mn, Co, Ti, V, and Cu were not significant, suggesting that these elements did not actively participate in the degradation reaction (Fig. 9(c–g)). The increase in the content of hydroxyl radicals in the O 1s spectrum can be attributed to the fact that FeOOH is a common reaction product of Fe in dye degradation (Fig. 9(h)).[57] Thus, as the main active site in the dye degradation process, Fe led to an increase in the proportion of hydroxyl radicals on the surface of the alloy after the reaction. Furthermore, the concentration tests of released ions in the degraded solution showed that the release amounts of all elements complied with relevant standard requirements (Table 1).[33]

Table 1 Leached metal ion concentrations (in μg L^{-1}) after the degradation of Orange II over FeMnCoTiVCu HEAPs

	Fe^{2+}	Mn^{2+}	Co^{2+}	Ti^{2+}	V^{2+}	Cu^{2+}
Orange II	122	427	2	4	18	16

3.5. Density functional theory (DFT) calculations

The 3d band distribution of HEAPs is closely related to the types of elements present. By controlling the types and quantities of elements to fill the energy regions near the Fermi level, HEAPs with excellent absorption across the entire solar spectrum can be obtained.[41,67]

Existing research has found that, compared to conventional binary or ternary alloys, the local density of states (LDOS) of atoms in high-entropy alloys loses the characteristic features of single elements due to the random arrangement of atoms and the diversity of LDOS. The electronic structures of different elements can exhibit the LDOS characteristics of other elements.[67–69] While these studies elucidate the 3d band distribution of high-entropy alloys with the same number of principal elements, they overlook the influence of the number of principal elements on the density of states in the 3d band distribution. This study reveals that as the number of principal elements increases, the shape of the 3d energy band gradually becomes broader and smoother. This characteristic indicates that by adjusting the number of elements in high-entropy alloys, the shape of the density of states can be effectively modulated.[70–73]

We calculated the density of states for transition metal elements such as Fe, Co, Mn, Ni, Ti, V, Cr, and Cu, along with the high-entropy alloy powders (HEAPs) synthesized from them, to elucidate the relationship between the density of states of the individual elements and that of the HEAPs. By employing a composition design based on equal molar ratios, we can intuitively compare the density of states of HEAPs with different

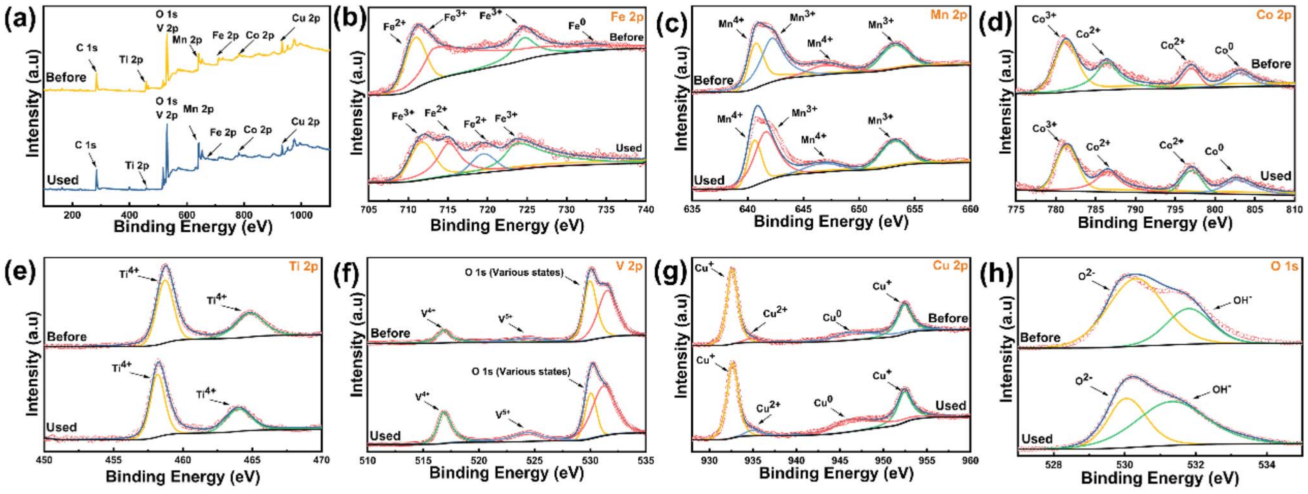

Fig. 9 XPS spectral analysis before and after degradation: (a) FeMnCoTiVCu HEAPs; (b) Fe 2p; (c) Mn 2p; (d) Co 2p; (e) Ti 2p; (f) V 2p; (g) Cu 2p; (h) O 1s.

compositions. Fig. 10(a) presents the results based on DFT calculations, showing that the 3d electrons of Fe, Mn, and Co are concentrated around the Fermi level, and these three elements have been demonstrated to possess good solar absorption properties.[45,74,75] We used the FeMnCo ternary alloy as a base and added other transition metal elements to alloy it, thereby adjusting the 3d band distribution of the alloy to enhance its solar absorption properties.

From Fig. 10(b–e), it can be observed that as the number of elements increases from four to eight, the 3d band distribution

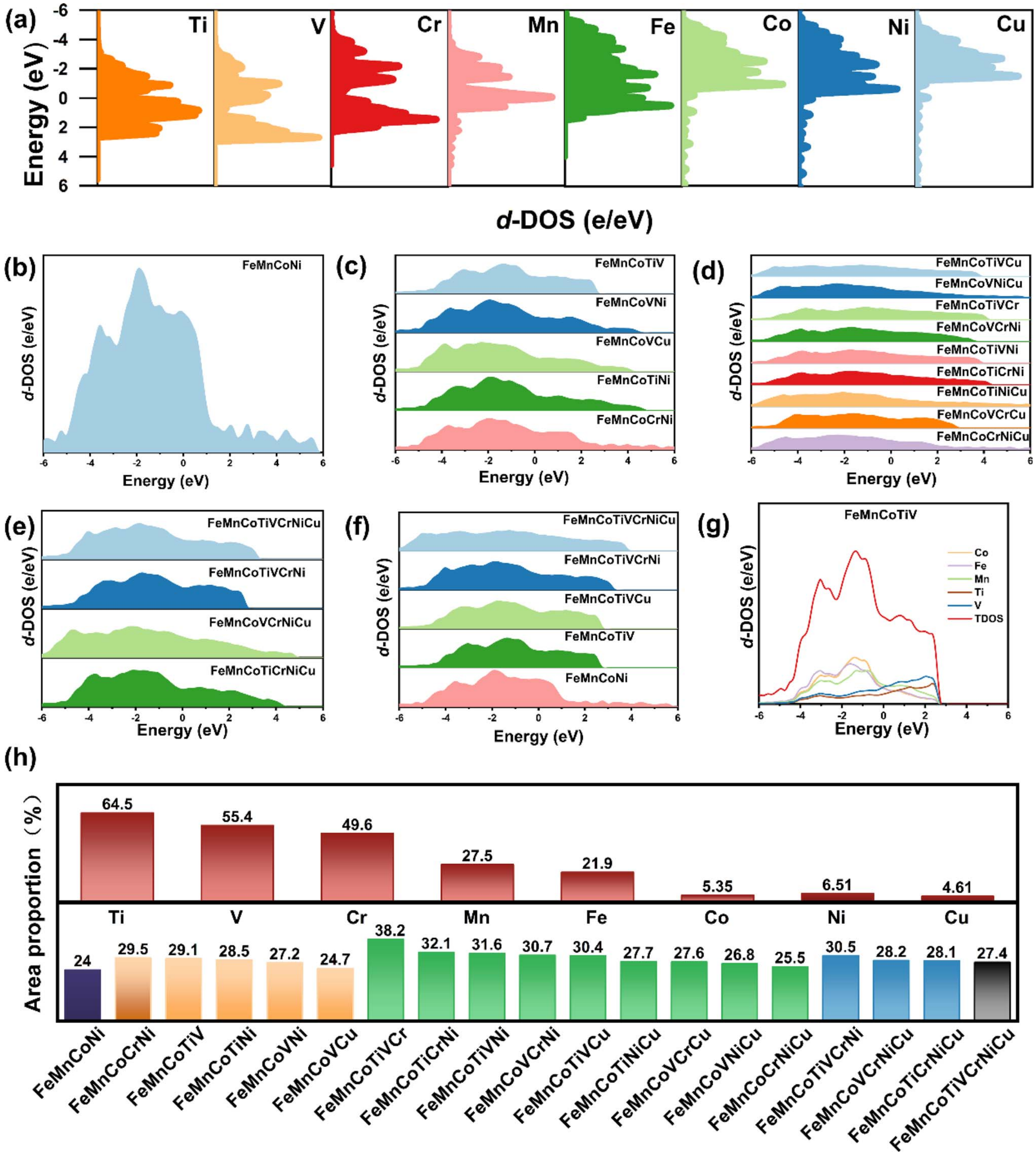

Fig. 10 Theoretical calculations of 3d HEAPs. (a) 3d band distributions of transition metals: Ti, V, Cr, Mn, Fe, Co, Ni, and Cu, respectively. (b) Quaternary HEAPs. (c) Quinary HEAPs. (d) Senary HEAPs. (e) Septenary HEAPs. (f) Octonary HEAPs. (g) 3d band distribution of different principal element HEAPs with the best light absorption performance. (h) The proportion of the area of the 3d electron distribution above the Fermi level to the total area of the 3d electron distribution in HEAPs.

of HEAPs gradually becomes wider and smoother. The 3d band distribution of the quaternary alloy remains somewhat steep above the Fermi level, but it becomes increasingly broad and smooth from the quinary alloy to the octonary HEAPs. HEAPs containing the same number of principal elements exhibit similarities in their 3d band distribution.

Fig. 10(f) shows the 3d band distribution of components with the best solar absorption performance among different principal element alloys. As the number of principal elements increases, the 3d band distribution of the octonary HEAPs of FeMnCoTiVCrNiCu becomes very broad and smooth. The 3d band distribution characteristics of FeMnCoTiVCrNiCu no longer match those of single elements, with the distribution range between −6 eV and +4 eV. The 3d band distribution of the solar-absorbing efficient FeMnCoTiV in the 3d band narrows to between −4 eV and +3 eV. When alloying based on the FeMnCo alloy, the electronic structures of other elements tend to become similar to those of Fe, Mn, and Co elements, leading to the DOS of the quinary high-entropy alloys being distributed around the Fermi level. As more principal elements are introduced, Fe, Mn, and Co no longer serve as the primary elements and fail to play a predominant assimilative role, causing the density of states in the high-entropy alloys to become broader and move further away from the Fermi level. Compared to other multi-principal element alloys, the density of states around the Fermi level in the quinary high-entropy alloys is more concentrated and uniform, with the 3d band distribution of FeMnCoTiV being the most concentrated and uniform around the Fermi level compared to other HEAPs with different principal element counts, thereby enhancing d–d transitions and improving solar absorption performance.[40,76,77]

The range of 3d band distribution in high-entropy alloys is influenced by the 3d band distribution of the constituent elements. However, most studies have been limited by the relatively small number of high-entropy alloy compositions examined, preventing a systematic comparison of the impacts of different elemental types on 3d band distribution. This study clarifies that different types of elements can cause the 3d band distribution to shift either above or below the Fermi level. Fig. 10(h) illustrates the ratio of the area of the 3d band distribution above the Fermi level to the total area of the 3d band distribution for all samples. In the powdered high-entropy alloys, the 3d band distribution of the added elements is primarily concentrated either above or below the Fermi level. After alloying, the main area of the 3d band distribution in the newly formed high-entropy alloy powder tends to shift correspondingly upward or downward relative to the Fermi level when compared to the original high-entropy alloy powder. For Ti, V, and Cr, the proportions of their 3d band distributions above the Fermi level are 64.5%, 55.4%, and 49.6%, respectively, all of which are higher than those of the other five elements. In contrast, the proportion for Cu is the lowest, at only 4.61%.

Adding Ti, V, and Cr can increase the proportion of the 3d band distribution above the Fermi level in high-entropy alloys, while the addition of Cu leads to a decrease in this proportion. In the FeMnCoNi alloy, the proportion of the 3d band distribution above the Fermi level is 24%. Following the addition of Ti, V, and Cr, the proportions for FeMnCoCrNi, FeMnCoTiNi, and FeMnCoVNi increase to 29.5%, 28.5%, and 27.2%, respectively. However, upon adding Cu to these three alloys, the proportions of the 3d band distribution above the Fermi level for FeMnCoCrNiCu, FeMnCoTiNiCu, and FeMnCoVNiCu decrease to varying extents. This trend is also applicable to other alloy compositions. When Ti, V, and Cr are simultaneously added, the proportion of the 3d band distribution above the Fermi level in FeMnCoTiVCr is the highest among all samples, reaching 38.2%. However, when the Cr element is replaced with Cu, this proportion decreases to 30.4% for FeMnCoTiVCu. Among the seven-element alloy series, FeMnCoTiVCrNi exhibits the highest proportion of 3d band distribution above the Fermi level, while the proportions for FeMnCoTiVCrNiCu and FeMnCoTiCrNiCu decline upon the addition of Cu.

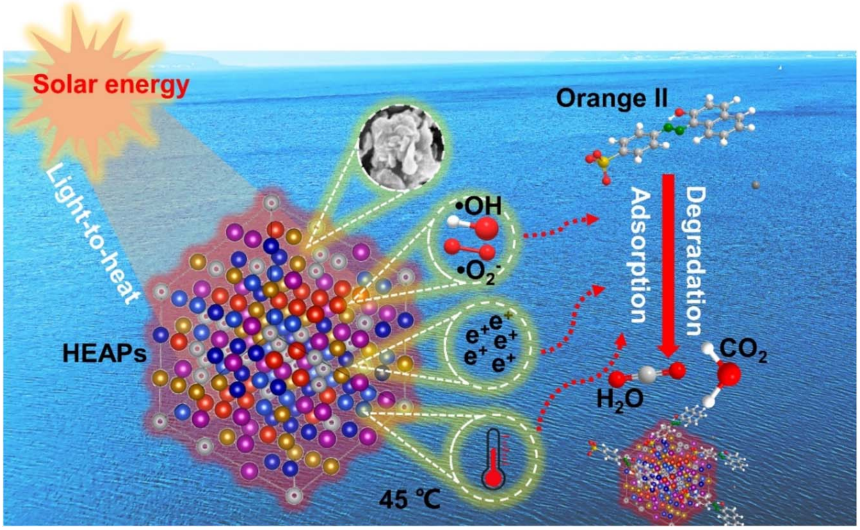

Fig. 11 Schematic illustration of the degradation mechanism of HEAPs under sunlight.

Fig. 10(g) shows the projected density of states for the FeMnCoTiV HEAPs. It can be observed that in the FeMnCoTiV, the density of states for Ti and V is primarily distributed above the Fermi level, while the density of states for Fe, Mn, and Co is mainly concentrated around the Fermi level. This electronic distribution of titanium and vanadium effectively fills the density of states near the Fermi level, thereby enhancing the d–d transitions in the high-entropy alloy and significantly improving its light absorption performance.

The above experiments prove that by adjusting the number and types of elements, we can effectively modulate the 3d band distribution of high-entropy alloys, thereby further optimizing the material's solar absorption performance.[78]

Based on the above discussions, we elucidated the degradation mechanism of HEAPs on Orange II (Fig. 11). During the corrosion process, HEAPs release a significant amount of positive charges, which combine with negatively charged Orange II molecules through electrostatic interactions, forming electrostatic adsorption. The high specific surface area of the HEAPs and the porous sponge structure formed during the degradation process not only shorten the diffusion distance of electrons but also enhance the adsorption capacity for Orange II molecules. Furthermore, under light irradiation, the HEAPs can not only convert solar energy into thermal energy to increase the solution temperature and accelerate the degradation process but also generate $^{\bullet}$OH and $^{\bullet}O_2^-$ as strong oxidants, decomposing the dye into H_2O and CO_2.

4. Conclusions

This study successfully synthesized a series of FeMnCo-based HEAPs with excellent photothermal conversion properties using mechanical alloying methods. Specifically, FeMnCoTiV HEAPs exhibited the highest solar absorption efficiency (85.6%) across the solar spectrum (200–2500 nm), allowing for efficient water heating (up to 45 °C) under visible light irradiation.

This study explores the efficacy of photothermal materials, HEAPs, in antibacterial applications and dye degradation. The HEAPs of FeMnCoNi, FeMnCoTiV, and FeMnCoTiVCrNi exhibited antibacterial rates ranging from approximately 78.5% to 84% against *E. coli*, and 73.5% to 78% against *S. aureus*. All HEAPs demonstrated an improvement in the degradation rate of methyl orange dye by about 5% to 10% due to electrostatic adsorption. And the release of copper ions plays important roles in antibacterial processes.

Theoretical calculations indicate that as the number of elements in HEAPs increases, the shape of the 3d band distribution becomes smoother and more dispersed, accounting for the broad solar absorption range of HEAPs. The incorporation of Ti and V raises the 3d band distribution towards the Fermi level, contributing to the high absorption efficiency of HEAPs. This study provides insights for the development of solar-driven wastewater treatment materials.

Data availability

The data supporting this article have been included as part of the ESI.†

Conflicts of interest

There are no conflicts to declare.

Acknowledgements

This work was supported by the Science and Technology Project of Jiangsu Province (BE2023719, BK20241352) and Suzhou Science and Technology Project (SJC2023005, SZS2023023).

References

1 S. Song, Y. Zhang, T. Yu and J. Yang, *J. Mater. Sci. Technol.*, 2024, **202**, 129–139.
2 Y. Jia, C. Shan, W. Fu, S. Wei and B. Pan, *Water Res.*, 2023, **242**, 120289.
3 A. Bendi, C. Vishaka, V. Chanchal, Yogita, Chinmay and N. Raghav, *Chem. Eng. J.*, 2024, **490**, 151373.
4 Z. Zhang, N. Abidi and L. Lucia, *J. Mater. Sci. Technol.*, 2023, **159**, 81–90.
5 X. Yang, L. Wang, J. Tong, X. Shao, Y. Feng, J. Zhou, Y. Han, X. Yang, F. Ding, J. Zhang, Q. Li, G. Li, A. R. Zimmerman and B. Gao, *Chemosphere*, 2023, **313**, 137410.
6 L. Sun, Y. Mo and L. Zhang, *Chemosphere*, 2022, **294**, 133801.
7 K. Zhang, R. Cen, H. Moavia, Y. Shen, A. Ebihara, G. Wang, T. Yang and R. Sakrabani, *Chem. Eng. J.*, 2024, **492**, 152310.
8 H. Yu, M. Hu, Z. Hu, F. Liu, H. Yu, Q. Yang, H. Gao, C. Xu, M. Wang, G. Zhang, Y. Wang, T. Xia, L. Peng and Y. Wang, *Carbohydr. Polym.*, 2022, **286**, 119298.
9 D. T. C. Nguyen, T. V. Tran, P. S. Kumar, A. T. M. Din, A. A. Jalil and D. N. Vo, *Environ. Chem. Lett.*, 2022, **20**, 1421–1451.
10 J. Huang, H. Pang, Z. Liu, X. Wang, C. Zhang, W. Zhang, S. Liu and W. He, *Chem. Eng. J.*, 2024, **491**, 151971.
11 W. Liu, F. Huang, Y. Liao, J. Zhang, G. Ren, Z. Zhuang, J. Zhen, Z. Lin and C. Wang, *Angew. Chem., Int. Ed.*, 2008, **47**, 5619–5622.
12 Y. Yu, S. Li, J. Lu, F. Xi, X. Chen, D. Wu, W. Ma and R. Deng, *Chem. Eng. J.*, 2024, **499**, 155933.
13 W. Liu, F. Huang, Y. Wang, T. Zou, J. Zheng and Z. Lin, *Environ. Sci. Technol.*, 2011, **45**, 1955–1961.
14 Y. Wu, W. Zhou, L. Zhou, S. In, J. Lei, L. Wang, J. Zhang and Y. Liu, *Chem. Eng. J.*, 2023, **474**, 145267.
15 A. S. M. Nur, M. Sultana, A. Mondal, S. Islam, F. N. Robel, A. Islam and M. S. A. Sumi, *J. Water Process. Eng.*, 2022, **47**, 102728.
16 K. Xie, J. Fang, L. Li, J. Deng and F. Chen, *J. Alloys Compd.*, 2022, **901**, 163589.
17 G. Gao, Y. Yu, G. Zhu, B. Sun, R. He, A. Cabot and Z. Sun, *J. Energy Chem.*, 2024, **99**, 335–364.
18 C. Sun, H. Liu, Z. Xu, Y. Wu, K. Yan, J. Ju, J. Jiang, F. Xue, J. Bai and Y. Xin, *J. Mater. Sci. Technol.*, 2024, **176**, 13–24.
19 A. A. Deshmukh and R. Ranganathan, *J. Mater. Sci. Technol.*, 2025, **204**, 127–151.
20 Y. Lin, S. Luo, W. Zhao, Q. Sun, J. Cong, P. Li, P. Li and S. Yan, *J. Energy Chem.*, 2024, **98**, 441–471.

21 D. Zhang, D. Shi, F. Wang, D. Qian, Y. Zhou, J. Fu, M. Chen, D. Qiu and S. Jiang, *J. Alloys Compd.*, 2023, **966**, 171536.

22 A. Fu, Z. Xie, J. Wang, Y. Cao, B. Wang, J. Li, Q. Fang, X. Li, B. Liu and Y. Liu, *Mater. Sci. Eng., A*, 2024, **901**, 146547.

23 Q. Guo, H. Hou, K. Wang, M. Li, P. K. Liaw and Y. Zhao, *npj Comput. Mater.*, 2023, **9**, 185.

24 W. Al Zoubi, R. A. K. Putri, M. R. Abukhadra and Y. G. Ko, *Nano Energy*, 2023, **110**, 108362.

25 Y. Zhou, X. Shen, T. Qian, C. Yan and J. Lu, *Nano Res.*, 2023, **16**, 7874–7905.

26 Y. Yao, Q. Dong, A. Brozena, J. Luo, J. Miao, M. Chi, C. Wang, I. G. Kevrekidis, Z. J. Ren, J. Greeley, G. Wang, A. Anapolsky and L. Hu, *Science*, 2022, **376**, 151.

27 J. Q. F. H. Yezeng He, *Chem. Eng. J.*, 2024, **492**, 152145.

28 Q. Dong, J. Jiang, J. Zhang, Z. Hu and X. Zhang, *J. Magnesium Alloys*, 2024, DOI: 10.1016/j.jma.2024.07.023.

29 Z. Y. Lv, X. J. Liu, B. Jia, H. Wang, Y. Wu and Z. P. Lu, *Sci. Rep.*, 2016, **6**, 34213.

30 S. Wu, Y. Wang, Y. Wang, F. Fan, Y. Pan and N. Yin, *J. Mater. Res. Technol.*, 2023, **26**, 8972–8982.

31 L. Miao, Y. Guo, Z. Liu, Y. Li, J. Zhu and L. Wu, *Chem. Eng. J.*, 2023, **467**, 143451.

32 N. Wang, *Surf. Interfaces*, 2022, **33**, 102265.

33 S. Das, M. Sanjay, S. Kumar, S. Sarkar, C. S. Tiwary and S. Chowdhury, *Chem. Eng. J.*, 2023, **476**, 146719.

34 X. Zhang, Y. Yu, B. Ren, Z. Liu, T. Li, L. Wang and Z. Qiao, *Mater. Today Commun.*, 2023, **35**, 105946.

35 B. Yu, T. Juma, H. Wang, X. Bao, X. Cao, Z. Wang, R. Wang, X. Yang, T. Ning, G. Liang, Y. Cao, T. Zhang and Z. Guan, *J. Mater. Sci. Technol.*, 2023, **141**, 209–220.

36 C. Yang, H. Feng, X. Chen, Y. Han, H. Li, D. Xu and F. Wang, *J. Mater. Sci. Technol.*, 2023, **139**, 92–102.

37 J. He, Q. Wei, S. Wang, S. Hua and M. Zhou, *Biomaterials*, 2021, **271**, 120734.

38 Y. Jiang, J. Li, X. Zhen, C. Xie and K. Pu, *Adv. Mater.*, 2018, **30**, 1705980.

39 Y. Li, Y. Liao, L. Ji, C. Hu, Z. Zhang, Z. Zhang, R. Zhao, H. Rong, G. Qin and X. Zhang, *Small*, 2022, **18**, 2107265.

40 Y. Liao, Y. Li, R. Zhao, J. Zhang, L. Zhao, L. Ji, Z. Zhang, X. Liu, G. Qin and X. Zhang, *Natl. Sci. Rev.*, 2022, **9**, 124–134.

41 Y. Li, Y. Liao, J. Zhang, E. Huang, L. Ji, Z. Zhang, R. Zhao, Z. Zhang, B. Yang, Y. Zhang, B. Xu, G. Qin and X. Zhang, *Angew. Chem., Int. Ed.*, 2021, **60**, 27113–27118.

42 H. Yu, Q. Li, Y. Hu, K. Li, K. M. Reddy, G. Xie, X. Liu and H. Qiu, *Nano Lett.*, 2023, **23**, 10554–10562.

43 Z. Lei, B. Hu, P. Zhu, X. Wang and B. Xu, *Nano Energy*, 2024, **122**, 109307.

44 Q. Wan, F. Zhang, Y. Xiong and C. Shang, *Ceram. Int.*, 2023, **49**, 35496–35508.

45 H. Liu, Y. Li and J. Wei, *Chem. Eng. J.*, 2024, **480**, 147892.

46 L. Ren, W. Zhou, L. Wang, K. Lin, Y. Xu, J. Wu, Y. Xie and H. Fu, *Sci. Bull.*, 2023, **68**, 2760–2768.

47 M. Yang, X. Cai, C. Wang, P. Li, S. Chen, C. Liu, Y. Wang, K. Qian, Q. Dong, F. Xue, C. Chu, J. Bai, Q. Liu and X. Ni, *ACS Appl. Mater. Interfaces*, 2024, **16**, 35964–35984.

48 E. Zhou, D. Qiao, Y. Yang, D. Xu, Y. Lu, J. Wang, J. A. Smith, H. Li, H. Zhao, P. K. Liaw and F. Wang, *J. Mater. Sci. Technol.*, 2020, **46**, 201–210.

49 M. Fu, Y. Shen, H. Zhou, X. Liu, W. Chen and X. Ma, *J. Mater. Sci. Technol.*, 2023, **142**, 22–33.

50 J. Gu, F. Duan, S. Liu, W. Cha and J. Lu, *Chem. Rev.*, 2024, **124**, 1247–1287.

51 S. Huang, H. Yao, K. Yue, H. Xiao, H. Liao, C. Hu, J. Tang and J. R. Zhao, *Vacuum*, 2024, **224**, 113177.

52 Z. Jia, Q. Wang, L. Sun, Q. Wang, L. C. Zhang, G. Wu, J. H. Luan, Z. B. Jiao, A. Wang, S. X. Liang, M. Gu and J. Lu, *Adv. Funct. Mater.*, 2019, **29**, 1807857.

53 S. Tiwari, W. H. Ryu, K. J. Kim and E. S. Park, *J. Alloys Compd.*, 2023, **961**, 171027.

54 L. Ji, S. Y. Peng, Z. G. Zheng, J. L. Zuo, D. C. Zeng, Z. G. Qiu, M. Xiao, J. W. Chen and H. Y. Yu, *J. Alloys Compd.*, 2020, **815**, 152347.

55 Y. Sun and S. Dai, *Sci. Adv.*, 2021, **7**, eabg1600.

56 M. Deleu, H. Razafindralambo, Y. Popineau, P. Jacques, P. Thonart and M. Paquot, *Colloids Surf., A*, 1999, 3–10.

57 J. Wei, Z. Zheng, L. Huang, Z. Qiu, Q. Xia, S. Zhou, X. Tong and D. Zeng, *Colloids Surf., A*, 2023, **656**, 130388.

58 L. Miao, Y. Guo, Z. Liu, Y. Li, J. Zhu and L. Wu, *Chem. Eng. J.*, 2023, **467**, 143451.

59 T. Wang, Y. Wang, N. Wang, S. Xu, Z. Han and Y. Wang, *Mater. Lett.*, 2021, **283**, 128817.

60 P. Martin, C. Aguilar and J. M. Cabrera, *J. Mater. Res. Technol.*, 2024, **30**, 1900–1928.

61 C. Zhang, Z. Zhu and H. Zhang, *J. Phys. Chem. Solids*, 2017, **110**, 152–160.

62 Y. Xiao, Z. Wang, B. Yao, M. Cao and Y. Wang, *Small*, 2024, **20**, e2304843.

63 A. Lassoued and J. F. Li, *J. Phys. Chem. Solids*, 2023, **180**, 111475.

64 N. Zhang, Y. Wang, M. Liu, T. Cheng, Z. Xing, Z. Li and W. Zhou, *Small*, 2024, e2400652.

65 S. Das, M. Sanjay, A. R. Singh Gautam, R. Behera, C. S. Tiwary and S. Chowdhury, *J. Environ. Manage.*, 2023, **342**, 118081.

66 Y. Liu, Z. Chen, X. Yang, J. Zhang, Z. Sun, Y. Chen and F. Liu, *J. Mater. Res. Technol.*, 2021, **15**, 256–267.

67 D. Wu, K. Kusada, Y. Nanba, M. Koyama, T. Yamamoto, T. Toriyama, S. Matsumura, O. Seo, I. Gueye, J. Kim, L. S. Rosantha Kumara, O. Sakata, S. Kawaguchi, Y. Kubota and H. Kitagawa, *J. Am. Chem. Soc.*, 2022, **144**, 3365–3369.

68 Y. Maruta, K. Kusada, D. Wu, T. Yamamoto, T. Toriyama, S. Matsumura, O. Seo, S. Yasuno, S. Kawaguchi, O. Sakata, Y. Kubota and H. Kitagawa, *Chem. Commun.*, 2022, **58**, 6421–6424.

69 H. Wu, Q. Lu, Y. Li, J. Wang, Y. Li, R. Jiang, J. Zhang, X. Zheng, X. Han, N. Zhao, J. Li, Y. Deng and W. Hu, *Nano Lett.*, 2022, **22**, 6492–6500.

70 D. Wu, K. Kusada, T. Yamamoto, T. Toriyama, S. Matsumura, I. Gueye, O. Seo, J. Kim, S. Hiroi, O. Sakata, S. Kawaguchi, Y. Kubota and H. Kitagawa, *Chem. Sci.*, 2020, **11**, 12731–12736.

71 Y. Zhai, X. Ren, B. Wang and S. F. Liu, *Adv. Funct. Mater.*, 2022, **32**, 2207536.

72 J. Ren, L. Chen, H. Wang and Z. Yuan, *Inorg. Chem. Front.*, 2024, **11**, 2029–2038.

73 P. Li, B. Wu, K. Du, Z. Liu, E. Gao, H. Yin and D. Wang, *ACS Sustain. Chem. Eng.*, 2023, **11**, 14246–14254.

74 J. A. Delgado Notario, D. López Díaz, D. McCloskey and J. M. Caridad, *Adv. Funct. Mater.*, 2024, 2401599.

75 L. Zhu, L. Tian, S. Jiang, L. Han, Y. Liang, Q. Li and S. Chen, *Chem. Soc. Rev.*, 2011, **52**, 7389–7460.

76 Y. Li, L. Yang, Y. Liao, R. Zhao, L. Ji, R. Su, D. Xu and F. Wang, *Adv. Funct. Mater.*, 2023, 7389–7460.

77 T. Gao, R. Zhao, Y. Li, Z. Zhu, C. Hu, L. Ji, J. Zhang and X. Zhang, *Adv. Funct. Mater.*, 2022, **32**, 2204370.

78 Q. Raza, I. Bibi, F. Majid, S. Kamal, S. Ata, A. Ghafoor, M. I. Arshad, S. H. Al-Mijalli, A. Nazir and M. Iqbal, *J. Ind. Eng. Chem.*, 2023, **118**, 469–482.